NAVIGATION USING SERENDIPITOUS STAR-TRACKER OBSERVATIONS AND ON-BOARD DATA PROCESSING

Rachel Mamich[*], Daniel Kucharski[†], Renato Zanetti[‡], Moriba K. Jah[§], Elvis D. Silva[¶], Jacob D. Griesbach[‖], and Joshua Fine[**]

A majority of spacecraft are equipped with star trackers to estimate their attitude. With the ever growing number of objects orbiting the Earth, these star trackers often serendipitously capture space objects in the images that they take to estimate the spacecraft's attitude. This study aims to assess the feasibility of using these measurements in order to estimate the state of an observer spacecraft. To do so, the visibility of these space objects is analyzed as well as the performance of a navigation algorithm written to utilize these measurements. The study found that using serendipitous measurements of space objects is indeed feasible when the observer is in an orbit where there are a large number of space objects that are visible. Observers in low Earth orbits were shown to have success with this navigation algorithm. Observers in approximately geostationary orbits have a fairly limited number of space objects that are visible.

INTRODUCTION

The Global Positioning System (GPS) revolutionized spacecraft navigation by providing accurate and inexpensive onboard localization. GPS navigation is ubiquitous, and can result in a single source of failure of many satellite systems. Accordingly, an area of considerable current interest is what to do when a satellite enters a GPS-denied or degraded environment. Reliance on ground-based navigation is certainly an attractive backup solution, but it requires availability of tracking stations which are currently oversubscribed by the rapid increase of the number of artificial satellites (ASOs, Anthropogenic Space Objects) in Earth orbit. Alternatively, an onboard solution that is gaining considerable interest is the use of optical navigation.[1–3] Onboard situational awareness cameras have been proposed for this use but they are often not designed for navigation purposes and might not provide the accuracy required. Attitude cameras, such as star trackers, are an appealing solution as they are often accurate to a few tens of arc-seconds.

To a star camera, ASOs look like dim stars, and can therefore be used as reference targets for angles-only navigation. The attitude of the camera can be easily derived based on the stars captured

---
[*]Graduate Student, Aerospace Engineering and Engineering Mechanics, UT Austin, 2617 Wichita St, Austin, TX 78712.
[†]Research Associate, Aerospace Engineering and Engineering Mechanics, UT Austin, 2617 Wichita St, Austin, TX 78712.
[‡]Assistant Professor, Aerospace Engineering and Engineering Mechanics, UT Austin, 2617 Wichita St, Austin, TX 78712.
[§]Associate Professor, Aerospace Engineering and Engineering Mechanics, UT Austin, 2617 Wichita St, Austin, TX 78712.
[¶]Advanced Systems Manager, Advanced Technologies and Missions, Ball Aerospace, 1600 Commerce St, Boulder, CO 80301.
[‖]Chief Architect, Space Domain Awareness, National Intelligence Systems, Ball Aerospace, 1600 Commerce St, Boulder, CO 80301.
[**]Advanced Systems Manager, Ball Aerospace, 1600 Commerce St, Boulder, CO 80301.

in images, and the position and velocity can be determined from observing known ASOs whose ephemeris are uploaded in an onboard catalog. This paper presents a feasibility study to evaluate the viability and accuracy of this approach.

The analysis is developed in two parts: visibility and navigation. The visibility study focuses on the detection of artificial satellites by a star camera sensitive element.

The navigation study evaluates the performance of an Extended Kalman Filter (EKF) to estimate the position and velocity of an observing satellite given the estimated attitude of the observer, angles only observations of ASOs, and the ASOs respective ephemeris information. While previous work in this area has shown promise in establishing baseline feasibility,[4] this study aims to add more realism to the analysis and expected performance. We couple the EKF design and performance study with a visibility and accuracy analysis starting from star camera parameters. Additionally, this study aims to bring in state of the art uncertainty estimates for the ASO catalog used in the algorithm to allow for more realistic error estimates on the observer's state estimates.[5]

ASO VISIBILITY

The optical detection of the satellites by a space-based imaging sensor can be achieved if the distant objects within the sensor's Field-of-View (FOV) are sunlit and bright enough to exceed the detection threshold of the receiver. The performance analysis and probability of the space object detection has been analyzed in the literature[6,7] and, in the case of the space-based sensing, depends on a series of factors describing the physical and optical properties of the observed objects, specification of the receiver as well as the range to the target and the geometrical configuration between Sun-Satellite-Receiver. The irradiance of an incoming flux collected by the space-based sensor $I\left[\frac{W}{m^2}\right]$ can be predicted by:

$$I = I_0 \left(\frac{R_0}{R_1}\right)^2 \frac{A}{R^2} \Psi$$

where I_0 is the calibrated flux constant (Figure 1) calculated as an integral of the solar spectral irradiance $E_{Sun}(\lambda)$ over the detector's spectral bandwidth from λ_0 to λ_1 at $\Delta\lambda = 1nm$ steps with the wavelength dependent quantum efficiency $\eta_q(\lambda)$ and the receiver optics efficiency $\eta_D(\lambda)$:

$$I_0 = \sum_{\lambda=\lambda_0}^{\lambda_1} E_{Sun}(\lambda) \eta_q(\lambda) \eta_D(\lambda)$$

$E_{Sun}(\lambda)$ is defined by the reference profile ASTM G173-03 and represents intensity of the solar flux arriving at the satellite (before reflection) at the distance of $R_0 = 1AU$ and has to be scaled to the actual Sun - satellite distance R_1 according to the inverse-square law.
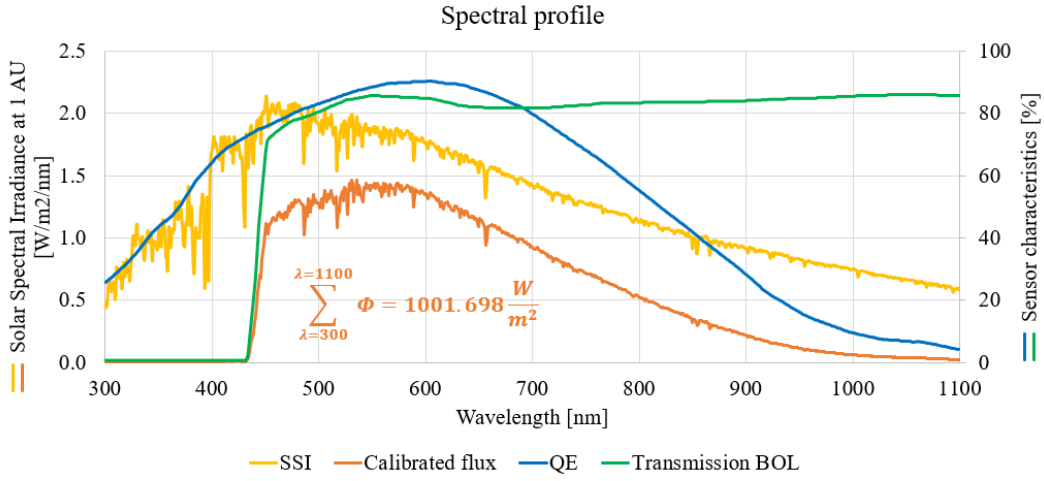
Figure 1: Spectral characteristics of the solar flux and the sensor. Solar Spectral Irradiance model is given by ASTM G173-03 Reference Spectra.

The calibrated flux constant for the given characteristics of the optical sensor over the spectral response range 300-1100 nm equals to $I_0 = 1001.698 \frac{W}{m^2}$ at 1AU at the Beginning-of-Life (BOL). When solar irradiation impacts a satellite surface, a fraction of the incident flux can be reflected towards the receiver located at the distance R from the sunlit object. In this work the satellite is modelled as a Lambertian sphere of a diffuse reflection coefficient C_d and a cross-sectional area A. The historical radar cross-section (RCS) records of 32081 satellites (http://www.celestrak.com/satcat) allow constructing a statistical representation of RCS with respect to the orbital apogee (Figure 2); assuming a cannonball model, the RCS curve can represent a physical cross-section A.
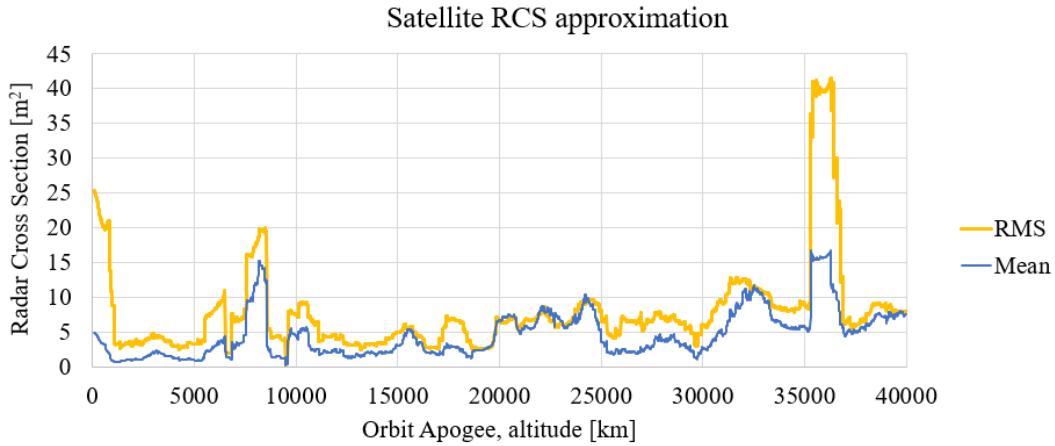

Figure 2: Mean radar cross-section of 32081 satellites at the apogee altitudes up to 40,000 km above Earth surface.

The intensity of a Lambertian reflection depends on the phase reflection function[6] :

$$\Psi = \frac{C_d}{\pi}(\sin(\alpha) + (\pi - \alpha)\cos(\alpha))$$

3

where α is the phase angle between the satellite centered direction vectors towards the Sun and the imaging sensor. The visual magnitude of a satellite within the receiver's FOV can be predicted by:

$$mag_{sat} = mag_{Sun} - 2.5log\left(\frac{I}{I_{Sun}}\right)$$

where the Sun apparent magnitude is $mag_{Sun} = -26.74$, and the solar constant $I_{Sun} = 1362\frac{W}{m^2}$. In the simulations the reflection coefficient C_d is set constant at 0.2.

The detection thresholds used in this work are those of real sensor hardware. Specifically, the investigated space sensor can detect $mag_{sat} = 8.7$ at 98 ms exposure time and $mag_{sat} = 12.7$ at the long exposure of 5 s.

For long exposure times, as LOS pointing during sensor integration periods misalign with targets and background stars, their respective signatures will "streak" across the focal plane and hence, the resulting image. Since streaking results in signal energy residing across multiple pixels, the overall per pixel energy signal-to-noise-ratio (SNR) is reduced as it divides (roughly evenly). For single (best) pixel detection algorithms, streaking can produce a significant degradation to tracking low-SNR targets (and stars).

To counter the degraded SNR effects associated with signal streaking, velocity matched filtering (VMF),[8, 9] can be employed to effectively compensate for signal motion within a frame (intra-frame motion) and/or across multiple frames (inter-frame motion). VMF works by postulating a family of motion hypotheses for potential targets located/centered at any given image pixel. Each motion hypothesis translates to a specific streak direction and rate that, if a target were present with such motion, would define how that target energy would manifest across pixels and frames. With this, the motion hypothesis is convolved with the sensor's point spread function (PSF) to produce a replica of the expected target energy as it would be expected. This replica response is equivalent to a matched filter that is then convolved across the image/frame data (after background noise normalization is performed). The results of this convolution can be simply per pixel thresholded for detection, where the detection with maximum SNR is chosen over all the motion hypotheses.

VMF can produce detections that would normally not be visible for target streaks that have SNR beneath the image noise floor. By integration SNR accumulated over multiple pixels and frames, VMF can pull signal energy above detection thresholds.

Because many motion hypotheses are usually necessary, VMF can be very computationally complex to implement. However, dedicated onboard FPGAs can be implemented to host the necessary replica generation and convolutions.

While VMF can be used for star detection as well as ASO detection, VMF is generally not needed for stars, as typically SDA sensor FOVs are wide enough to detect a sufficient number of stars for frame registration without VMF. If VMF is to be used for star detection, typically the LOS motion relative to sidereal motion is known, and can then be implemented with far fewer, perhaps even a single, motion hypothesis.

NAVIGATION DESIGN

The algorithm employed for this feasibility study is an Extended Kalman Filter (EKF).[10] EKFs are widely accepted as an industry standard as a great compromise between computational simplicity and performance in the presence of mild nonlinearities. The full state vector **x** includes the

observer's position $\mathbf{r}$ and velocity $\mathbf{v}$, the rotation vector parameterization of the attitude error about the camera head units (CHU) of the two star trackers $\boldsymbol{\theta}_1$ and $\boldsymbol{\theta}_2$, and the estimated error of the observed ASOs' positions $\boldsymbol{\epsilon}_i$, $i = 1...8$. The observer spacecraft is assumed to have two separate CHUs with a 90° separation as this is a common industry practice. The number of ASO processed at any one time is limited to no more than eight. The position and velocity of the observer spacecraft and the estimated error about the observed ASOs' positions are expressed in the inertial frame. The parameterization of the attitude error about the camera head units (CHU) of the star trackers are expressed in the CHU1 and CHU2 frames respectively.

The position and velocity of the observer are initialized based on the last known position and velocity of the spacecraft, for example from a ground update or prior to loss of GPS, their initial 1σ uncertainties are set to 100 m and 0.1 $\frac{m}{s}$, respectively. The inertial attitude of each star camera is assumed to be determined from the stars in its field of view and used as is from the EKF. To account for the star camera attitude errors the EKF design includes the effects of attitude errors by including them as "consider" state.[11] The filter's attitude error state is initialized to be zero at the beginning of each run and its associated 1σ uncertainty 50 arc-seconds along bore-sight and 17 arc-seconds cross-bore-sight. The "true" error of each star camera measurement is simulated as a first order Gauss-Markov process with a time constant of 60 s.

The catalogue from ASTRIAGraph[5] with its associated uncertainties is used by the EKF. The "true" catalogue error is drawn once per ASO.

The EKF algorithm is composed of two different phases, the time propagation and the measurement update. Measurements are assumed to be available once per second, the propagation section carries the estimated of state and covariance matrix forward in time by one second using a fourth order Runge-Kutta (RK) algorithm. The dynamics model employed by the filter to propagate the position and velocity includes central gravity as well as J_2, J_3, and J_4 zonal harmonics. The equations that govern this motion can be found below.

$$\mathbf{a}_{TBP} = -\frac{\mu}{r^3}\mathbf{r}$$

$$\mathbf{a}_{J2} = -\frac{3}{2}J_2\left(\frac{\mu}{r^2}\right)\left(\frac{R_{Earth}}{r}\right)^2 \begin{bmatrix} \left(1 - 5\left(\frac{z}{r}\right)^2\right)\frac{x}{r} \\ \left(1 - 5\left(\frac{z}{r}\right)^2\right)\frac{y}{r} \\ \left(3 - 5\left(\frac{z}{r}\right)^2\right)\frac{z}{r} \end{bmatrix}$$

$$\mathbf{a}_{J3} = -\frac{1}{2}J_3\left(\frac{\mu}{r^2}\right)\left(\frac{R_{Earth}}{r}\right)^3 \begin{bmatrix} 5\left(7\left(\frac{z}{r}\right)^3 - 3\left(\frac{z}{r}\right)\right)\frac{x}{r} \\ 5\left(7\left(\frac{z}{r}\right)^3 - 3\left(\frac{z}{r}\right)\right)\frac{y}{r} \\ 3\left(10\left(\frac{z}{r}\right)^2 - \frac{35}{3}\left(\frac{z}{r}\right)^4 - 1\right) \end{bmatrix}$$

$$\mathbf{a}_{J4} = -\frac{5}{8}J_4\left(\frac{\mu}{r^2}\right)\left(\frac{R_{Earth}}{r}\right)^4 \begin{bmatrix} \left(3 - 42\left(\frac{z}{r}\right)^2 + 63\left(\frac{z}{r}\right)^4\right)\frac{x}{r} \\ \left(3 - 42\left(\frac{z}{r}\right)^2 + 63\left(\frac{z}{r}\right)^4\right)\frac{y}{r} \\ -\left(15 - 70\left(\frac{z}{r}\right)^2 + 63\left(\frac{z}{r}\right)^4\right)\frac{z}{r} \end{bmatrix}$$

Additionally, the estimated error about the observed ASOs' positions is held constant at zero in the propagation step.

The covariance matrix is propagated using the state transition matrix. In this study, the propagation time is small enough that the state transition matrix can be approximated by the matrix exponential $\Phi = e^{-A\Delta t}$. Where A is the Jacobian of the state propagation function with respect to the state space. Then the covariance is propagated using the equation below.

$$P^-(k+1) = \Phi P^+(k)\Phi^T + Q$$

A higher fidelity dynamics is used to simulate the "true" orbit and the difference between the two is accounted for by including into the filter process noise with power spectral density of 1e-6m^2/s^3 for low Earth orbit cases and 1e-7m^2/s^3 in the radial and transverse directions and 1e-12 m^2/s^3 in the normal direction for the near geostationary case discussed further in the numeric results section.

The measurement update function is called only if at least one ASO is visible for at least one CHU. The measurements used in the filter are the angles describing the ASO's location in the field of view with respect to the bore-sight center. The equations for the measurements can be found below in Equation .

$$A = \arctan\left(\frac{\hat{\rho}_x}{\hat{\rho}_z}\right)$$
$$B = \arctan\left(\frac{\hat{\rho}_y}{\hat{\rho}_z}\right)$$

Where $\hat{\rho}$ is the unit vector defined in the star tracker frame that defines the relative position vector of the ASO with respect to the observer. ρ can be found using the equation below.

$$\rho = C_i^c \left(\mathbf{r}_{ASO} - \mathbf{r}\right)$$

Where C_i^c is the direction cosine matrix that defines the change of coordinates from the inertial frame to the camera frame of the star tracker, $\mathbf{r}_{ASO}$ is the inertial position vector of the observed ASO propagated to the time of measurement using the latest information in the catalog, and $\mathbf{r}$ is the inertial position vector of the observer spacecraft. C_i^c is calculated by taking the inertial attitude estimate with respect to the body frame and rotating it to the known offset of the CHU camera frame for the CHU that took the observation.

In the measurement update it is assumed that the measurements have already been associated with a cataloged ASO object. The data association algorithm is left as future work. When a new ASO object enters the field of view, the algorithm retrieves an estimate of the covariance of the uncertainty associated with the ASO's ephemeris. When applying the measurement update to the system it should be noted that many of the state elements are treated as consider parameters and thus were not updated with the measurement. The only states that are indeed updated during the measurement update step are the position and velocity of the observer spacecraft. This was achieved by zeroing the rows of the Kalman gain matrix that corresponded to the consider parameters. The calculation of the Kalman gain matrix can be seen below.

$$K = P^-(k+1)H^T(k+1)P_{yy}(k+1)^{-1}$$
$$K[7:,:] = 0$$

Where $P_{yy}(k+1)$ is the residual covariance and K[7:, :] corresponds to rows 7-36 of the Kalman gain matrix. In summary, only position and velocity are estimated, all other states are considered.[12]

It should be noted that underweighting was utilized in order to reduce the update of the covariance bounds to compensate for nonlinear effects.[13] While there are more refined methods of applying underwriting, a common ad hoc method implementation is to add $0.2HPH^T$ to the residual covariance. This can be seen below.

$$P_{yy}(k+1) = (1+0.2)\, H(k+1)P^-(k+1)H^T(k+1) + R(k+1)$$

This increases the residual covariance and thus causes a smaller change to be affected into the state update, underweighting the measurement. The measurements themselves are corrupted by zero-mean, additive Gaussian white noise with standard deviation 1/3 pixels. This is a conservative value chosen for simplicity. In reality the measurement noise will between 1/3 and 1/10 of a pixel depending on the SNR of the received target detection; i.e., brighter ASOs will have smaller error than dim ones. After the underweighting and consider parameter adjustments are made, the state update is carried out as it is done in a traditional EKF. This can be seen below.

$$x^+(k+1) = x^-(k+1) + Ky$$

Where y is the measurement residual and $x^-(k+1)$ is the propagated state prior to the measurement update. The covariance update is carried out using the Joseph form to avoid numeric precision issues. This can be seen below.

$$P^+(k+1) = (\mathbb{1} - KH(k+1))P^-(k+1)(\mathbb{1} - KH(k+1))^T + KR(k+1)K^T$$

NUMERICAL RESULTS

In order to assess the validity of using serendipitous observations of cataloged ASOs for navigational purposes, a truth model is required. In the truth model the observer spacecraft is assigned initial orbital elements and propagated using a variable time step RK45 propagator. The dynamics equations passed to the RK45 include a full 8x8 gravitational model for the Earth, drag effects, solar radiation pressure, and third body effects from the sun and moon. These are some of the most dominant perturbing forces acting on spacecraft in orbit around the Earth. This dynamics propagation is used to generate "truth" trajectories. The maximum number of measurements for a single time step allowed is 8, this is done to keep the size of the state vector manageable.

In order to develop a baseline to compare against, a nominal trajectory is selected. The nominal trajectory for this study is a nearly circular, low Earth orbit (LEO) with an inclination of $45°$, right ascension of the ascending node of $0°$, and argument of perigee of $0°$. This orbit is at a common altitude (1000km) and eccentricity (1e-6) as satellites in LEO orbits typically have nearly circular orbits due to drag effects. This nominal orbit is first used to establish what the ideal placement of the star cameras relative to the orbit frame and by extension the body frame (assuming the spacecraft keeps a constant attitude with respect to the orbit frame). The results of this test can be seen in Figure 3.
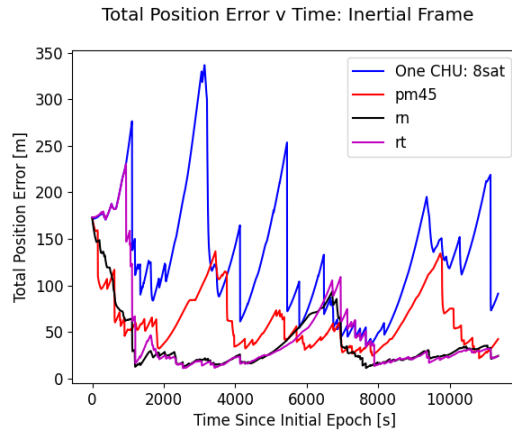
Total Position Error v Time: Inertial Frame

Figure 3: Total position errors over time for varying star tracker orientations with the observer in its nominal orbit.

The different total position errors in Figure 3 are as follows:

- One CHU: 8sat, one star tracker with its bore-sight pointed in the radial direction. A maximum of 8 ASOs measurements are processed at any time.

- pm45, one star tracker with its bore-sight pointed 45° forward with respect to the radial direction, in the orbital plane and the other pointed -45° with respect to the radial direction. A maximum of 4 ASOs measurements per star camera are processed at any time.

- rn, one star tracker with its bore-sight pointed in the radial direction and the other pointed in the orbit normal direction. A maximum of 4 ASOs measurements per star camera are processed at any time.

- rt, one star tracker with its bore-sight pointed in the radial direction and the other pointed in the transverse direction. A maximum of 4 ASOs measurements per star camera are processed at any time.

It can clearly be seen that the configurations where the star trackers are placed in the radial and orbit normal directions have the smallest total error on average. This makes sense as the transverse direction is approximately in the velocity direction of the observer and thus tends to be the largest contributor to the total position uncertainty. With the optical measurements used here, there is no observability in the direction of the bore-sight. This means placing the star trackers in the radial and orbit normal directions allows the observers' transverse direction to be observable with measurements from both star trackers. Thus the RN configuration is the most desirable configuration and is set to be the nominal star tracker configuration.

After the nominal configuration is established, three separate tests are conducted. The first is a Monte Carlo test that varied the initial state estimate of the system, the noise applied to each measurement, and the noise about the attitude estimate of the star trackers. The next test is an error budget analysis to gain a better understanding of the sources of error included in the covariance values around the observers' state. The last The last test is to analyze the number of objects in the field of view when the visual magnitude is limited to a certain thresholds. To gain an understanding of how useful this algorithm will be for varying capabilities of different star trackers.
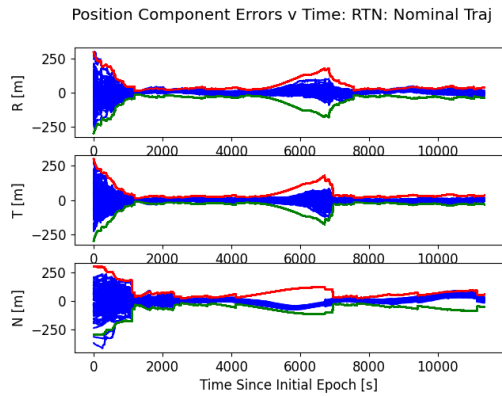
Nominal Trajectory Results

Figure 4: Position component errors and filter's predicted 3σ uncertainty from a 100 run Monte Carlo.
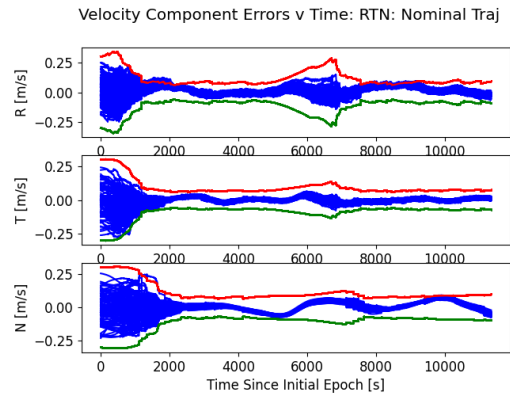
Figure 5: Velocity component errors and filter's predicted 3σ uncertainty from a 100 run Monte Carlo.

In Figures 4 and 5 it can be seen that the 3σ uncertainty about the position and velocity of the observer can be estimated down to about 50 m and 0.1 m/s in each direction during most of the orbit, but an occasional drop in visible ASOs at around 6000 seconds of simulation time causes the uncertainty to grow.

In Figure 6 it can be seen that during times where measurements are plentiful, the sources of error for the position are fairly evenly matched, and during times of measurement sparseness the process noise is the dominant term. This is a good indication that the filter is tuned properly.

An important design decision is the aperture time used in the camera image. While a longer time allows for detecting dimmer objects up to magnitude 12.7 with a few seconds of aperture, it also creates streaking and hence reduces measurement accuracy.

Figure 7 shows the EKF's accuracy when restricting the magnitude of the visible ASOs from 8.7 to 12.7. It can be seen that there is not a large difference in the total position error when restricting the visual magnitude to be brighter than 12.7 compared with restricting the visual magnitude to be brighter than 11.7. Additionally, there is not a huge jump once the brightness is restricted to be brighter than 10.7 or below. Figure 8 depicts the magnitude of the ASOs as seen by the star camera and processed by the EKF as measurements. It should be noted that the measurement noise is kept at 1/3 pixel (1σ) for all cases, which is pessimistic for brighter objects as they can be seen with shorter exposure times and hence less streaking and more accuracy.
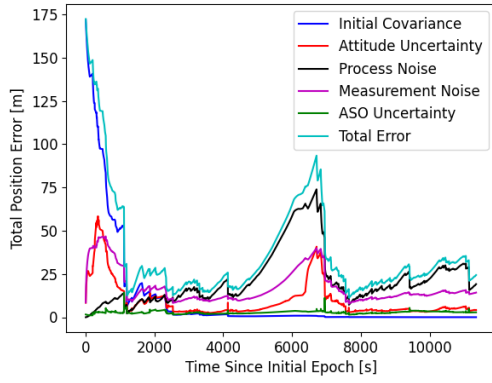
Figure 6: Total position error over time for the nominal orbit.
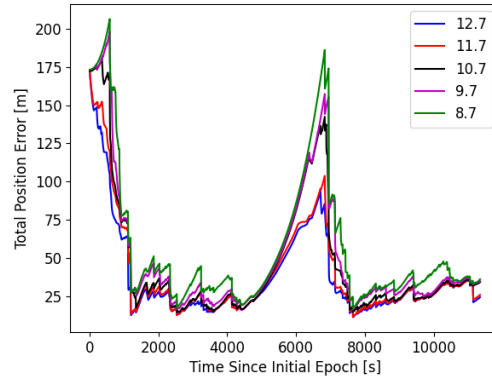
Figure 7: Error budget plot for various thresholds of visibility for measurements.
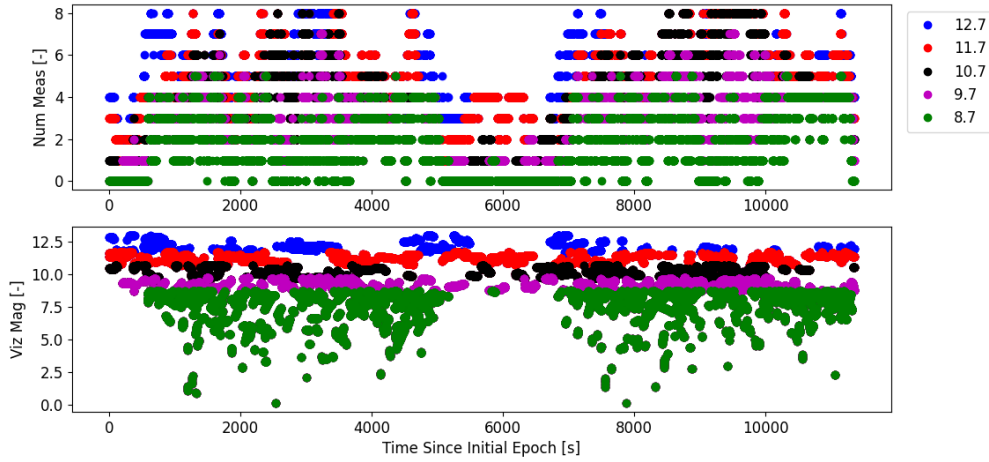

Figure 8: Plots of the number of objects in view over the test as well as the corresponding visual magnitude's of each observation.

Rotated Nominal Trajectory

To be sure that the nominal trajectory is not a unique edge case, the nominal trajectory is taken and effectively rotated about the Earth by changing the initial right ascension of the ascending node of the observer.
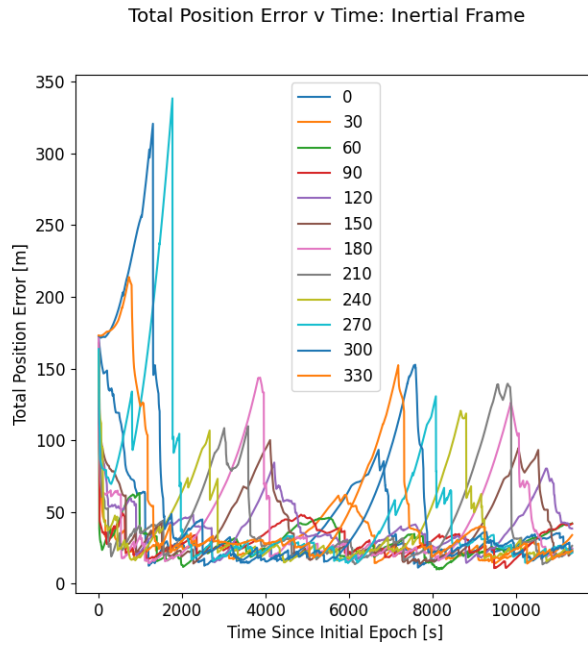
Figure 9: RMS position error over time for the rotated nominal orbits.

The legend in Figure 9 indicates the initial right ascension of the ascending node in degrees. It can be seen that the nominal trajectory has very similar behavior to the other similar orbits tested. All of the peaks in the various total position errors correspond to gaps in the measurement set and/or the dynamics causing the uncertainty to grow. This amount of variation is to be expected and the overall trend is fairly consistent.

Sun Synchronous Trajectory Results

The sun synchronous orbit is placed in a similar altitude to the nominal orbit, but to be a sun synchronous orbit, the inclination is adjusted according to the equation below.

$$i = \arccos\left(\frac{-2a^{\frac{7}{2}}\dot{\Omega}(1-e^2)^2}{3R_{Earth}^2 J_2\sqrt{\mu}}\right)$$

11
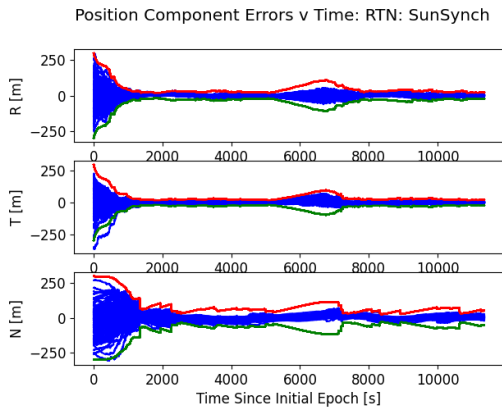
Figure 10: Position component errors and error bounds from a 100 run Monte Carlo.
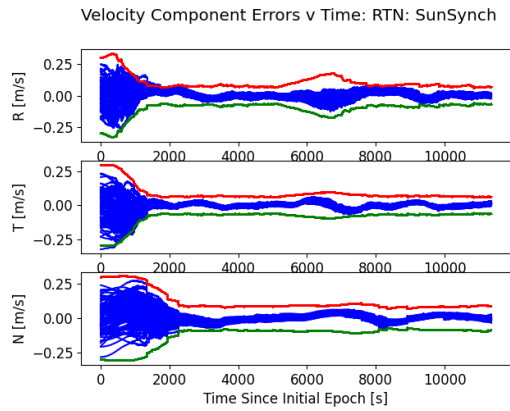

Figure 11: Velocity component errors and error bounds from a 100 run Monte Carlo.
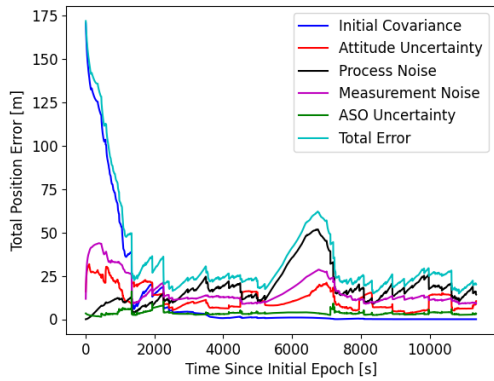
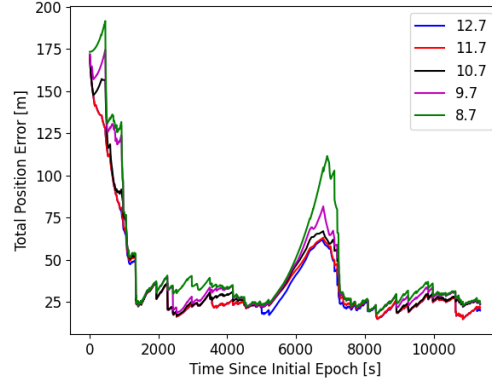**Figure 12**: Total position error over time for the sun synchronous orbit.

Figure 13: Error budget plot for various thresholds of visibility for measurements.

In Figures 10 and 11 it can be seen that, similar to the nominal case, the uncertainty about the position and velocity of the observer can be estimated down to about 50 m and 0.1 $\frac{m}{s}$ in each direction.

In Figure 12 similar behavior to to the nominal case can be seen. During times where measurements are plentiful, the sources of error for the position are fairly evenly matched, and during times of measurement sparseness the process noise is the dominant term. This is a good indication that the filter is tuned properly.

In Figure 13, it can be seen that there is not a large difference in the total position error when restricting the visual magnitude to be brighter than 12.7 compared with restricting the visual magnitude to be brighter than 9.7. This behavior is slightly different than the behavior seen in 7. This

is likely due to a higher density of measurements available in the sun synchronous orbit. In Figure 14 it can be seen that while being able to detect ASOs with low visibility (a high visual magnitude) is advantageous in that it allows for a greater number of ASOs to be utilized, there are still a large number of ASOs that are fairly bright with a visual magnitude of 8.7 or below.
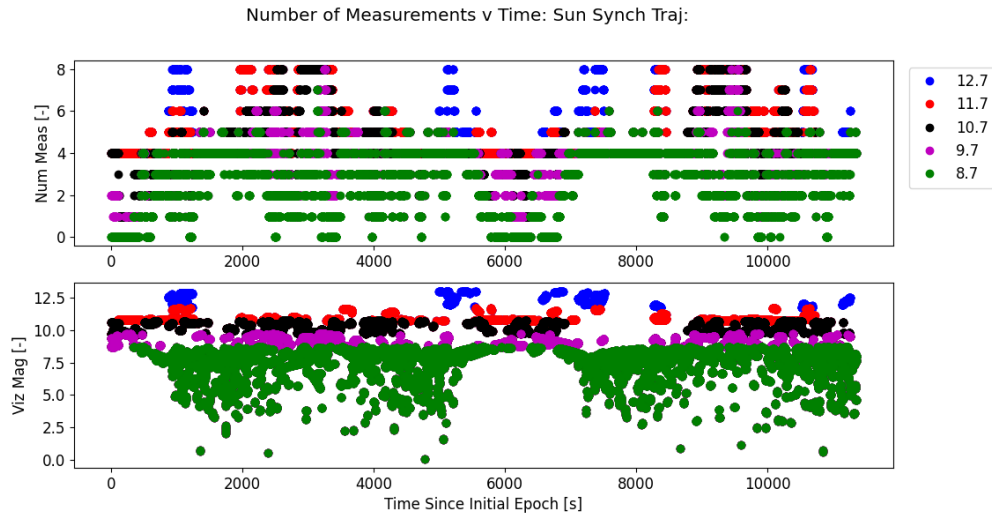

Figure 14: Plots of the number of objects in view over the test as well as the corresponding visual magnitude's of each observation.

Near-Geosynchronous Trajectory Results

The near-geosynchronous orbit tested is an orbit just below geosynchronous. The drift rate per day was set to be approximately $1.5°/day$. From this orbit geosynchronous ASOs can be seen in the field of view of the radial star tracker.
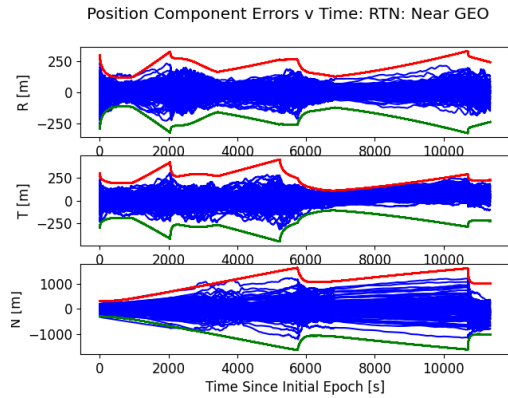

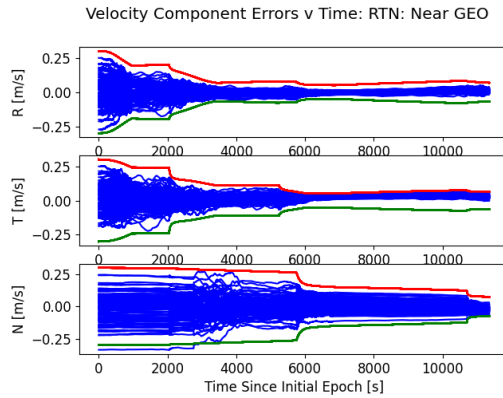**Figure 15**: Position component errors and error bounds from a 100 run Monte Carlo.

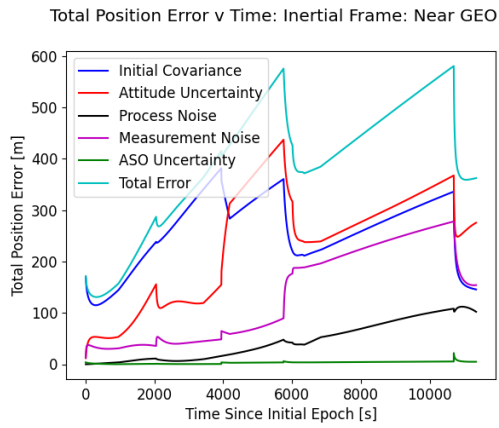**Figure 16**: Velocity component errors and error bounds from a 100 run Monte Carlo.

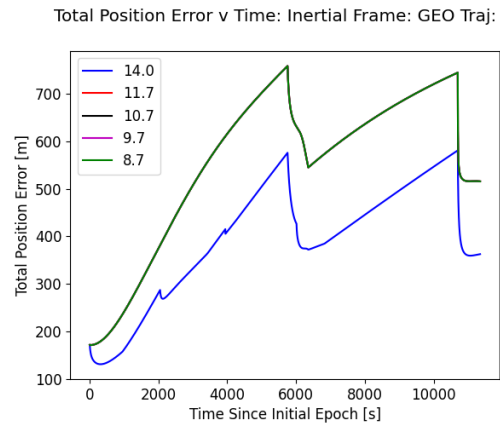**Figure 17**: Total position error over time for the near geosynchronous orbit.

Figure 18: Error budget plot for various thresholds of visibility for measurements.
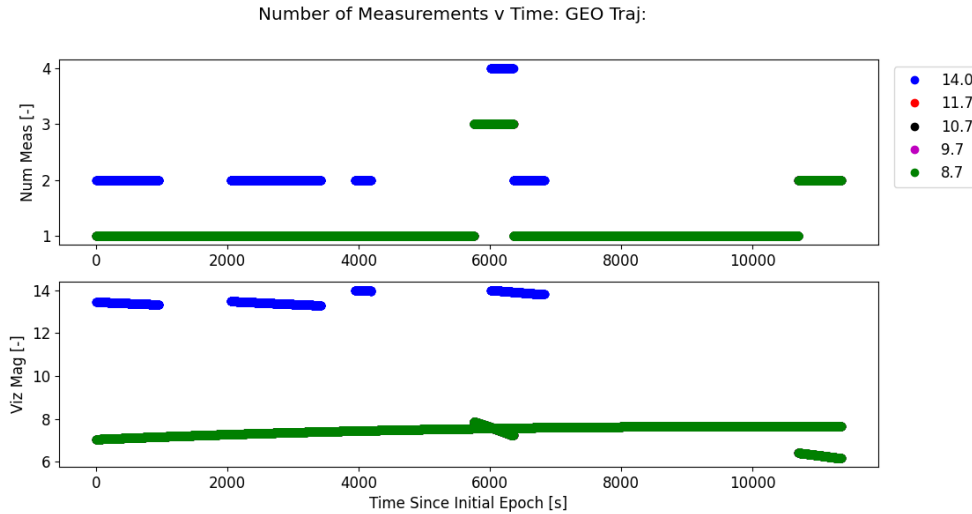

Figure 19: Plots of the number of objects in view over the test as well as the corresponding visual magnitude's of each observation.

In Figures 15 and 16 it can be seen that, the observer's state error is not reduced over the test period. This is likely due to the fact that there are not very many measurements taken over the test interval. Especially when comparing to the number of observations that are available in the LEO scenarios. This can clearly be seen comparing Figures 8 and 14 with Figure 19.

In Figure 17 is can be seen that the position errors primarily grow over time with an exception of a drop around 6000s where there are a larger number of ASO observations captured. The initial covariance of the system is one of the most dominant factors in the total error over time leading one to believe that this navigation technique may not be applicable to near geosynchronous orbits.

In Figure 19 it can be seen that the total number of satellites in the field of view never gets above 4. Additionally, there are a number of ASOs that are very dim, a visual magnitude over 14. When these are thrown out, the number of satellites in the field of view drops to only one satellite on average. In Figure 18, it can be seen that the position errors tend to increase over the testing period. That being said, this navigation algorithm may not be well suited for GEO or near GEO spacecraft due to limited numbers of ASOs in the field of view.

CONCLUSIONS

This study shows that when there are sufficient serendipitous observations available, they can indeed be used to estimate the state of the observer spacecraft. Spacecraft in LEO regimes are more likely to be able to utilize this approach due to there being a larger number of spacecraft in the field of view of the star trackers while keeping their boresights pointed away from the Earth to avoid dazzling the star trackers. Additionally, it was shown that this methodology will not provide useful results for observers in orbits with few visible spacecraft, as in the near geosynchronous orbit. That being said, this was a preliminary feasibility study. In future work, there are a variety of different avenues for improvement. First, and most obviously, the data association filter should be written to give the algorithm a more realistic view on which ASOs it can accurately matched to those in the catalog. Next, the algorithm should be tested over various altitudes in order to see when the number of objects in the field of view ceases to be useful. Finally, improvements to make the algorithm more realistic in weighting brighter measurements (and thus easier to find the centroid of for streaking purposes) should be made to see how trusting brighter observations would alter the outcome.

REFERENCES

[1] C. D'Souza, R. Inman, and K. Smith, "Artemis Optical Navigation Performance and Testing," *AIAA SciTech 2020 Forum*, Vol. 6, No. 10, 2020.

[2] V. H. Adams and M. Peck, "Interplanetary Optical Navigation," *AIAA Guidance, Navigation, and Control Conference*, Vol. 4, No. 8, 2016.

[3] A. Heintz and M. A. Peck, "Autonomous Optical Navigation for Resident Space Object Exploration," *AIAA Scitech 2020 Forum*, Vol. 6, No. 10, 2020.

[4] M. Driedger and P. Ferguson, "Feasibility Study of an Orbital Navigation Filter Using Resident Space Object Observations," *Journal of Guidance, Control, and Dynamics*, Vol. 44, No. 3, 2021, pp. 622–628.

[5] M. Jah, "AstriaGraph," https://astriagraph.spacetech-ibm.com/, March 2021.

[6] C. Früh and M. Jah, "Detection Probability of Earth Orbiting Objects Using Optical Sensors," *Proc. of AIAA/AAS Astrodynamics Specialists Conference*, 2014.

[7] F. Vitiello, "Performance Analysis of Space Surveillance Using Space Based Optical Sensors," *Aerotecnica Missili & Spazio*, Vol. 99, Dec. 2020, pp. 263–273, 10.1007/s42496-020-00063-1.

[8] P. S. Gural, J. A. Larsen, and A. Gleason, "Matched Filter Processing for Asteroid Detection," *The Astronomical Journal*, Vol. 130, October 2005, pp. 1951–1960.

[9] C. Zhai *et al*, "Detection of a Faint Fast-Moving Near-Earth Asteroid Using the Synthetic Tracking Technique," *The Astrophysical Journal*, Vol. 792, September 2014, pp. 60–73.

[10] A. Gelb, ed., *Applied Optimal Estimation*. Cambridge, MA: The MIT press, 1974.

[11] B. Tapley, B. Schutz, and G. Born, *Statistical Orbit Determination*. Elsevier Academic Press, 2004.

[12] S. F. Schmidt, "Application of State-Space Methods to Navigation Problems," *Advances in Control Systems*, Vol. 3, December 1966, pp. 293–340. doi: 10.1016/B978-1-4831-6716-9.50011-4.

[13] R. Zanetti, K. J. DeMars, and R. H. Bishop., "Underweighting Nonlinear Measurements," *Journal of Guidance, Control, and Dynamics*, Vol. 33, No. 5, 2010, pp. 1670–1675.